Triclinic phase: The link behind the structural transition in $V_{1-x}Mg_xO_2$

Raktima Basu,[1,*] V. Srihari,[2] T. R. Ravindran,[3] Sharat Chandra,[4] Himanshu Kumar Poswal,[2] and S. Dhara[1,†]
[1]*Surface and Sensors Studies Division, Materials Science Group, Indira Gandhi Centre for Atomic Research, Homi Bhabha National Institute, Kalpakkam 603102, India*
[2]*Synchrotron Utilization Section, Raja Ramanna Centre for Advanced Technology, Indore 452013, India*
[3]*Condensed Matter Physics Division, Materials Science Group, Indira Gandhi Centre for Atomic Research, Homi Bhabha National Institute, Kalpakkam 603102, India*
[4]*Defects and Damage Studies Division, Materials Science Group, Indira Gandhi Centre for Atomic Research, Homi Bhabha National Institute, Kalpakkam 603102, India*

(Received 1 December 2023; revised 16 April 2024; accepted 18 April 2024; published 10 May 2024)

Metal to insulator (MIT) phase transition accompanied by a structural phase transition (SPT) makes VO_2 a potential material for investigations into a strongly correlated transition metal oxide system. It undergoes a high-temperature metallic to a low-temperature insulating phase. The MIT is associated with the SPT from the rutile tetragonal (R) to the monoclinic ($M1$) phase. The structural transition occurs between $M1$ and R via two other insulating metastable phases, namely, monoclinic ($M2$) and triclinic (T). It has gained tremendous attention because of the half century old "chicken and egg" debate over the roles played by lattice distortion and electron-electron correlation. Despite several reports on the MIT and SPT between the R and $M1$ phases, a combined and detailed investigation of the relation among the various stable and metastable structural phases is still missing. We have studied the temperature- and pressure-induced structural phase transitions in the $V_{1-x}Mg_xO_2$ system by synchrotron x-ray diffraction and Raman spectroscopic measurements. We observe $M2 \rightarrow T \rightarrow M1$ phase transition upon compression, which is completely reversible upon decompression. The transition pressures for $M2 \rightarrow T$ and $T \rightarrow M1$ are observed to increase with the increase in doping concentration. The structural transitions from $M2$ to T to $M1$ in VO_2 are found to be second-order continuous phase transition. However, the temperature-driven $M2 \rightarrow R$ phase transition is found to be first order. We argue that Mott-type first-order metal to insulator transition prompts the MIT from R to $M2$, whereas a second-order structural phase transition/relaxation leads to the observation of $M2$ to $M1$ via the T phase. We further investigated the isothermal and isobaric Grüneisen parameters for individual phonon modes and relaxations of the samples related to their thermal expansion.

DOI: 10.1103/PhysRevB.109.184107

I. INTRODUCTION

Transition metal oxides have gained scientific and technological interest because of their ability to develop next generation power-efficient electrical and optical devices [1,2]. VO_2 is particularly important because it exhibits the metal to insulator phase transition (MIT) near room temperature. However, the MIT is accompanied by a structural phase transition (SPT) from a rutile tetragonal R (space group $P4_2/mnm$) to a monoclinic $M1$ ($P2_1/c$) phase [1–3]. Two other structural phases of triclinic, T ($P\bar{1}$), and monoclinic, $M2$ ($C2/m$), are also reported to evolve during the structural phase transition [4]. Phase stabilization of the metastable T (often denoted as monoclinic $M3$) and $M2$ at room temperature are reported by applying strain (tensile) along the rutile c axis (c_R) [5,6] or by doping with metals having lower valency than V^{4+} [7–9]. In various structural phases of VO_2, the major differences are in the arrangement of V atoms along the c_R axis. The R phase consists of equally spaced V chains (V-V distance being 2.86 Å) along the c axis (c_R), surrounded by an oxygen octahedron, forming a body-centered tetragonal lattice [10], whereas in the case of the $M1$ phase, the V atoms form pairs and the pairs are twisted along the c_R axis, with the unit-cell volume double that of the R phase [5,9,10]. In the $M1$ phase, the V-V separations are reported as 2.65 Å (bonding) and 3.12 Å (antibonding) along the $a_{M1} \leftrightarrow 2c_R$ axis. In the $M2$ phase, one chain of V atoms along the c_R axis forms a pair without twisting with V-V separations of 2.53 Å (bonding) and 3.25 Å (antibonding) along the $b_{M2} \leftrightarrow 2c_R$ axis. However, the nearest neighbor V chains do not pair but twist away from the c_R axis with a V-V separation of 2.93 Å [11]. The triclinic T is an intermediary phase between $M1$ and $M2$ [12]. Local strains prevent V-V dimers from twisting in one chain and consequently depairing the dimers in adjacent chains, promoting the $M2$ or T phase instead of the $M1$ phase [6,7,13]. Moreover, around the MIT, the resistivity decreases by four orders of magnitude [14,15], and infrared (IR) reflectivity increases in the high-temperature metallic phase [16–18]. As the MIT in VO_2 is also accompanied by a SPT

---

[*] Present address: Saha Institute of Nuclear Physics, 1/AF Bidhannagar, Kolkata 700064, India; raktimabasu14@gmail.com

[†] dhara@igcar.gov.in

and optical transition, the mechanism of this phenomenon is still under debate, whether it can be described in the Peierls scenario or by invoking electronic correlation following Mott physics [19–22]. Goodenough and Hong reported a qualitative explanation of the electronic transition of VO_2 [22]. In the low-temperature semiconducting phase of VO_2, V atoms form pairs in the rutile c (c_R) direction and the V-V pairs twist, which opens a gap of ~0.7 eV [11,12]. However, the Fermi level crosses the partially filled bands in the metallic phase, and the energy gap collapses. As reported theoretically by Zylbersztejn and Mott [10], Rice *et al.* [19], and Sommers and Doniach [23], the Coulomb repulsion is responsible for opening the energy gap in the semiconducting phases of VO_2. Moreover, in the $M2$ phase of VO_2, half of the V atoms form evenly spaced linear chains that can be regarded as one-dimensional (1D) Heisenberg chains according to nuclear magnetic resonance (NMR) [24] and electron paramagnetic resonance (EPR) [25] studies. In our previous studies [13,14,26], we have shown that the MIT in VO_2 is driven by electronic Coulomb repulsion and the physics of this system can be described by the Mott-Hubbard picture, where the Peierls (spin-phonon) instability arises subsequent to the MIT. The metal to insulator, as well as structural transition temperature (T_c) of VO_2, can be controlled in several ways, e.g., by invoking deformation [27], variation in the density of charge carriers [28], or doping [29]. Doping VO_2 with metals having lesser valency than +4 (Cr^{+3} [7], Al^{+3} [30], Ga^{+3} [9]) are reported to increase the T_c. On the other hand, T_c values are reported to increase for doping metals with valency of more than 4 (Ta^{+5}, Nb^{+5}, W^{+6}, Mo^{+6}) [31]. Moreover, doping with any divalent/trivalent metal ion produces adjacent V^{+5} (d^0) sites in the neighboring chains [13]. We have chosen Mg to stabilize the $M2$ phase by inducing local strain in the structures. A complete analysis of how Mg doping stabilizes the $M2$ phase is discussed in our previous reports [13,14]. Doping also initiates significant changes in the electrical, optical, and thermal properties of VO_2, making it applicable for electrical switching devices [32], smart windows with heat control [33], sensors for hazardous gas [34], and cathodes in batteries [35]. Furthermore, besides temperature and electric field [36], hydrostatic pressure [37] is also reported to initiate phase transition in VO_2. Though there are several reports on the MIT of VO_2, only a few reports [37,38] exist on the structural transitions between the various phases of VO_2.

In the present report, we have investigated the correlation among the various stable and metastable phases of VO_2 to clarify the roles played by lattice distortion and electron-electron correlation in the phase transitions. The order of the transitions, along with the isothermal and isobaric Grüneisen parameters and their relative contribution towards thermal expansion, are also analyzed in detail.

II. EXPERIMENT

$V_{1-x}Mg_xO_2$ microrods were grown by the vapor transport process on a high-purity (99.99%) alumina boat using mixed VO_2 powder and Mg powder (Sigma-Aldrich, 99%) as sources and Ar (99.9%) as the carrier gas. The synthesis was carried out for 3 h at 1100 K. The concentration of the Mg dopant was optimized by controlling the flow rate of the carrier gas using an MFC. Optimized flow rates of Ar (99.9%), e.g., 50, 80, and 100 SCCM (cubic centimeter per minute at STP) were used to synthesize samples S1, S2, S3, respectively, in the presence of Mg powder. High-pressure angle dispersive x-ray diffraction (XRD) experiments were performed using a Mao-Bell-type diamond anvil cell (DAC). The powdered sample, along with a ruby sphere [39,40] and the pressure transmitting medium (4:1 methanol:ethanol mixture [41]), was loaded in a preindented tungsten gasket. High-temperature XRD measurements were carried out with the STOE high-temperature stage attached to the Eurotherm PID controller. Raman spectra of the synthesized samples were recorded using a Raman spectrometer (inVia, Renishaw, UK) in the backscattering configuration with an Ar^+ laser (514.5 nm) as the excitation source and a thermoelectrically cooled CCD camera as the detector. For temperature-dependent Raman spectroscopic measurements, the sample was kept inside a temperature-controlled stage (Linkam, THMS600).

We used the electronic density functional theory (DFT), as implemented in the Vienna *ab initio* simulation package (VASP) [42,43], to calculate the total energy and equation of state (EOS) of the material. The bulk modulus for all the phases of VO_2 was calculated by fitting the DFT total energy vs volume data, generated for 21 isotropic changes in volume with ±10% range, to the third-order Birch-Murnaghan EOS.

III. RESULTS AND DISCUSSIONS

X-ray crystallographic structural studies of samples with different Mg dopants are shown in Fig. 1(a). All three samples, S1–S3, are found to be in the $M2$ phase of VO_2 (JCPDS No. 00-033-1441) [44,45]. The diffraction peaks corresponding to the (–201) and (201) planes of the $M2$ phase of VO_2 are observed at $\sim 2\theta = 13.38^\circ$ and 13.84°. The twin peaks indicate that these planes correspond to equivalent planes of the (011) plane of the monoclinic $M1$ phase [(110) plane of the R phase] [23]. The $M2$ phases of VO_2 are reported as the strained (tensile strain along the rutile c_R axis) state of the $M1$ phase of VO_2 [6]. However, in the current study, the substrate-induced strain can be neglected as the samples are synthesized on similar substrates, keeping all growth parameters identical except for the amount of carrier-gas exposure [20]. The percentage of Mg dopant was controlled by different flow rates of Ar gas. The dopants having different valency than V^{4+} may introduce strain in the sample and stabilize the $M2$ phase of VO_2 [14].

The percentage of Mg dopant in the samples was calculated from x-ray photoelectron spectroscopy (XPS) studies. The Shirley-type background-corrected XPS spectra for different elements with corresponding electronic transitions are shown in Fig. Suppl-1 in the Supplemental Material [46].

The dopant percentages for samples S1–S3 are calculated as 2.0, 2.2(1), and 2.3(2) at. %, respectively, from the area under the XPS curves considering appropriate sensitivity factors. We have collected the Raman spectra of the pristine samples to obtain further information about the phases present. The Raman spectra for the samples S1–S3 are collected at room temperature [Fig. 1(b)]. Eighteen Raman-active phonon modes are predicted by group theoretical analysis for $M2$ phases of VO_2, $1\,0A_g + 8B_g$ at the Γ point [4,26].

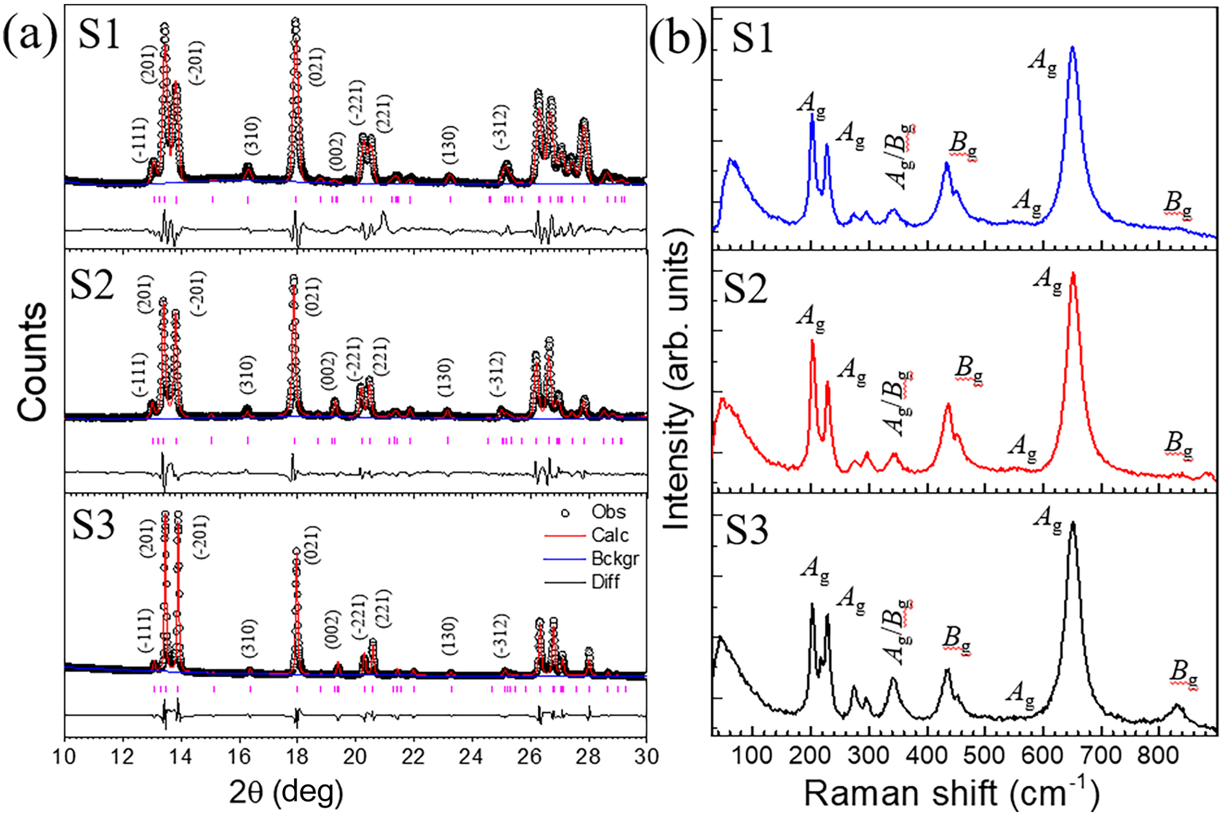

FIG. 1. (a) Refined x-ray diffraction patterns of the pristine samples S1–S3, indicating crystallographic (*hkl*) planes. (b) Typical Raman spectra of the samples S1–S3 with corresponding symmetry notations.

However, we observed ten vibrational modes for all the samples. Observed Raman modes at ~203 (A_g), 217(A_g), 229(A_g), 273 (either A_g or B_g; A_g/B_g), 297(A_g), 341(A_g/B_g), 432(B_g), 454(B_g), 651(A_g), and 831(B_g) cm^{-1} [Fig. 1(b)], confirm the presence of pure $M2$ phase of VO$_2$ [4,47].

As the metastable $M2$ phase is a strained (tensile) state of the $M1$ phase of VO$_2$, applying compressive stress may lead to a structural transition to the stable phase. To explore the structural changes with stress, we have collected the Raman spectra at room temperature as a function of quasihydrostatic pressure. With increasing pressure at 1 GPa, the Raman spectra for sample S1 show peaks at 200(A_g), 225(A_g), 267(A_g/B_g), 304(A_g), 343(A_g), 374(A_g/B_g), 409(A_g/B_g), 440(A_g/B_g), 501(A_g/B_g), 572(A_g), 636(A_g), and 828(B_g) cm^{-1} [Fig. 2(a)], which resemble the reported data for the $T(M3)$ phase [4,47]. The increase in the number of mode frequencies indicates a decrease in the symmetry. With further increase in pressure at 2.5(9) GPa Raman bands are observed at 190(A_g), 221(A_g), 258 (A_g/B_g), 307(A_g/B_g), 409(A_g), 465(A_g/B_g), 509(A_g/B_g), 627(A_g), 665(B_g), and 833(B_g) cm^{-1} [Fig. 2(a)], confirming the presence of pure $M1$ phase of VO$_2$ [28,48]. However, the main difference in various structural phases of VO$_2$ is in the arrangement of V atoms along the rutile c axis (c_R). The Raman modes ~200 and 230 cm^{-1}, referred to as ω_1 and ω_2, respectively, in Fig. 2, are due to V-V vibration as calculated from our DFT phonon modeling [14]. Therefore, we have focused on those modes to find the exact values for transition pressure. The vibration of V atoms gives rise to three Raman modes at 203, 217, and 229 cm^{-1} for the $M2$ phase, whereas in the case of the T phase, only two Raman modes are generated around 201 and 225 cm^{-1} due to the vibration of V atoms. The Raman mode at ~230 cm^{-1} (ω_2) remains almost at a constant frequency with pressure in all three phases, except for a little shift in the T phase. However, the mode frequency ~201 cm^{-1} (ω_1) in the T phase redshifts ~10 cm^{-1} until it reaches the $M1$ phase [denoted by the dashed line in Fig. 2(b)]. The mode shows a blueshift in the $M1$ phase with further increase in pressure [Fig. 2(b)]. The structural phase transitions from $M2 \rightarrow T$ and $T \rightarrow M1$ support the structural distortion of the strained $M2$ phase in reaching the stable $M1$ phase. A larger shift of the Raman mode at 203 cm^{-1} (2.95 cm^{-1}/GPa) than that of 229 cm^{-1} (0.68 cm^{-1}/GPa) with pressure confirms the distortion along c_R is responsible for the phase transition [26]. The Raman band observed at 651 cm^{-1} in the $M2$ phase of VO$_2$ arises due to V-O stretching vibration (ω_0). Another Raman mode ~578 cm^{-1} is found to evolve at 1 GPa, indicating the transition from the $M2$ to the T phase. The newly evolved mode frequency continues to blueshift and finally merges again in the $M1$ phase at 2.5 (9) GPa [denoted by dashed lines in Fig. 2(c)]. The ω_0 mode in $M2$ redshifts in T and again follows blueshifting with an increase in pressure for the $M1$ phase. For the sample S2, the structural transitions from the $M2$ to the T phase and the T to the $M1$ phase are observed at 1.2(3) and 2.6(2) GPa, respectively. The same for sample S3 is observed at 1.3 and

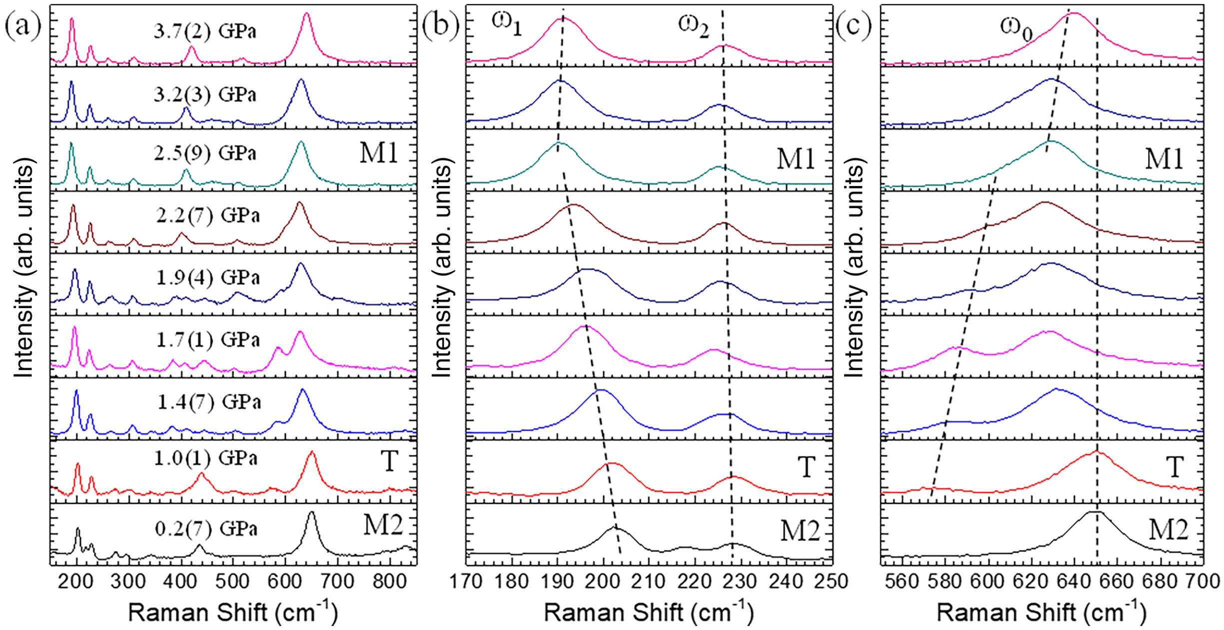

FIG. 2. Raman spectra of (a) sample S1 as a function of increasing quasihydrostatic pressure. The phases of VO_2 at the corresponding pressure are indicated. The evolution of Raman mode frequencies (b) ω_1 and ω_2 and (c) ω_0 with pressure. The dashed lines are guides to the eye.

3.0(4) GPa, respectively. In the pressure-releasing cycle, all three samples show reversible transitions from $M1$ to T to $M2$ with negligible hysteresis (Fig. Suppl-2 [46]). As samples S2 and S3 are doped with higher percentages of Mg, they are expected to be under more tensile strain than sample S1, and the transition pressure is expected to be high according to the phase diagram of VO_2 [6]. We have plotted the shift in Raman frequency as well as the change in the phonon lifetime with pressure. The Raman peak positions and full width at half maximum (FWHM) were extracted from the experimental data using Lorentzian peak fitting (after eliminating the spectrometer response function) for the whole pressure range. The phonon lifetime (τ) was calculated using the energy-time uncertainty relation $\tau = \hbar/\Delta E$, where ΔE is the full width at half maximum (FWHM) in cm^{-1} and $\hbar = 5.3 \times 10^{12}\ \mathrm{cm}^{-1}$ s. The pressure-dependent frequencies plot and variation in phonon lifetime are shown in the Supplemental Material [46]. Distinct changes in the spectra above 1 GPa for sample S1 are clearly seen in the ω vs P diagram (Fig. Suppl-3a [46]); (i) the Raman band at 218 cm^{-1} disappears; (ii) five new bands appear at 124, 378, 414, 504, and 576 cm^{-1}; (iii) the bands at 297, 341, and 435 cm^{-1} show blueshift; and (iv) the Raman bands at 203, 228, 273, 651, and 831 cm^{-1} show redshift. These are clear indications of a structural phase transformation from the $M2$ to the T phase of VO_2 [4,26]. With an increase in pressure ~2.5 GPa, again several changes are observed in the Raman spectra (Fig. Suppl-3 [46]); (i) the bands at 341, 415, and 576 cm^{-1} disappear; (ii) the bands at 127, 409, and 504 cm^{-1} show redshift; and (iii) the bands at 636 and 440 cm^{-1} show a blueshift. The phonon lifetime decreases with increasing pressure and shows an anomaly around the transition pressure (Fig. Suppl-3(b) [46]). These changes indicate another structural phase transition from the T to the $M1$ phase of VO_2 [28,48,49]. The Raman mode frequencies vary similarly with pressure for samples S2 and S3, except for slightly higher values of transition pressure. We have calculated the isothermal mode Grüneisen parameter [$\gamma_{i\mathrm{T}} = (K/\omega_i)(d\omega_i/\mathrm{d}P)|_T$; where K is the bulk modulus obtained from high-pressure XRD measurements described later] to find out the contribution from implicit anharmonicity of the Raman modes for sample S1 (tabulated in the Supplemental Material [46]). Table Suppl-I [46] lists the mode frequencies (ω_i) with the corresponding γ_{iT} with less than 10% error. Positive and negative values of Grüneisen parameters indicate the corresponding Raman modes contributing positively and negatively to thermal expansion, respectively [50]. The negative values of γ_{iT} for a few Raman modes in the $M2$ phase become zero or positive in the $M1$ phase, indicating the complete relaxation of the phase from the strain. To confirm the structural phase transition, wecarry out the XRD studies at room temperature as a function of quasihydrostatic pressure [Fig. 3(a)]. The observed XRD patterns are analyzed by the Rietveld refinement method using the GSAS program. The obtained lattice parameters, unit-cell volume, and average V-V distance in both the sublattices, along with fitting factors, are tabulated in Table Suppl-II [46]. In the absence of any pressure, all the samples maintain the $M2$ phase of VO_2, whereas, with an increase in pressure to 1.8(2) GPa in sample S1, the XRD pattern resembles the T phase of VO_2 [45]. With further increase in pressure to 3.4(2) GPa, the XRD pattern shows a transition to the $M1$ phase of VO_2 (JCPDS No. 04-007-1466) [23] [Fig. 3(a)] as also observed from high-pressure Raman studies (Fig. 2). As the structural phases of VO_2 are very close to each other, we need to concentrate on the diffraction pattern at low 2θ values for understanding the phase transitions [Fig. 3(b)]. The doublet peaks at $2\theta = 13.45\,^\circ$, and $13.85\,^\circ$ corresponding to the (201) and (20–1) planes of the $M2$ phase show an intensity flipping, indicating a change in symmetry to the T phase. The doublet peaks finally merge to the (011) plane of the $M1$ phase. We also observe the appearance of a tiny

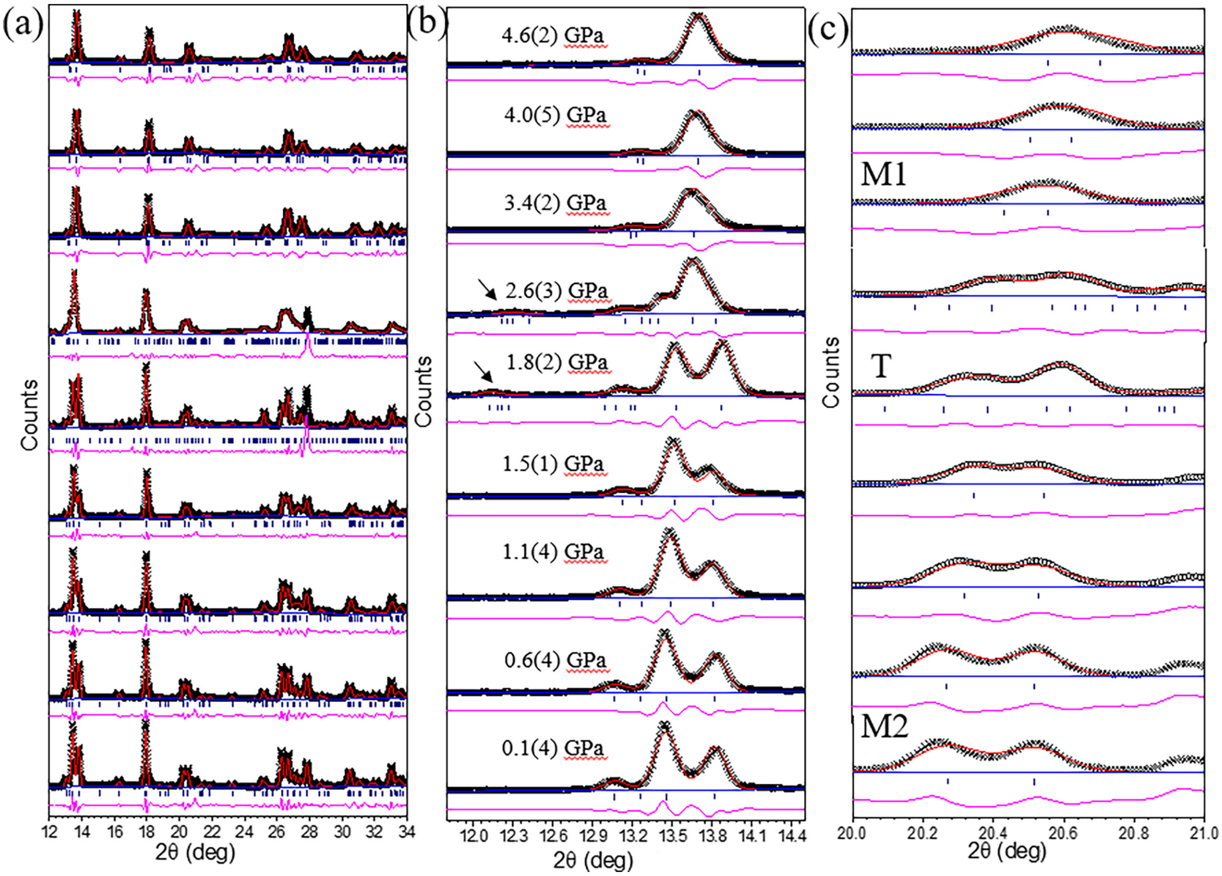

FIG. 3. (a) XRD pattern for sample S1, as a function of pressure (b), and (c) zoomed at lower 2θ values for better understanding of the transition. The phases of VO_2 at corresponding pressure are indicated.

diffraction line at a lower 2θ value [indicated by an arrow in Fig. 3(b)] in the T phase, which again disappears in the $M1$ phase [Fig. 3(b)]. The diffraction pattern at 1.8(2) GPa fits equally well by both monoclinic $M2$ and triclinic T phase with very little change in lattice parameters. That may be the reason behind referring to monoclinic $M3$ as the linking phase between $M1$ and $M2$ [45]. However, we observed a new line at $\sim 13.07^\circ$, which could not be fitted by the lattice parameters of the monoclinic phase. We also observed that the diffraction profile between 2θ values of 20°–21° could not be fitted by two planes of monoclinic $M2$ phase but rather fitted well by the (221), (2–21), (22–1), and (–221) planes of the triclinic T phase (Fig. Suppl-4a [46]). Therefore, we argue that the structural transition between $M2$ and $M1$ is via a continuous triclinic distortion. As the main difference in various structural phases of VO_2 is in the arrangement of V atoms along the rutile c_R axis, we focus on the variation of V-V distances in both sublattices (Table Suppl-II [46]). The V-V distances at ambient pressure ($M2$ phase) are found to be 2.5458 and 2.9603 Å in two sublattices (named sublattices 1 and 2 in Table Suppl-II [46]). With the increase in pressure, the V-V distances in both the sublattices start to decrease initially. However, after 1.5 GPa, the V-V distance in sublattice 1 starts to increase, whereas that in sublattice 2 continues to decrease. The V-V distances become equivalent at 3.4 GPa ($M1$ phase) and keep on decreasing with an increase in pressure thereafter. In the case of sample S2, the structural phase transitions from $M2$ to T and T to $M1$ are observed at 1.8(5) and 3.8(5) GPa, respectively. The phase transition pressure for $M2 \rightarrow T$ and $T \rightarrow M1$ in sample S3 are observed at 1.91 and 4.0 GPa, respectively. The XRD patterns for the samples are compared after the pressure is released, and the initial structure is found to be recovered (Fig. Suppl-4b [46]). However, we could not catch the T phase in pressure-releasing cycles due to very low values of transition pressures.

The structural transition from T to $M1$ is reported as a discontinuous transition by Mitrano *et al.* [37] because of the observed mixed-phase behavior in XRD and Raman studies. They also reported that the normalized unit-cell volume does not show any discontinuity around the phase transition, which contradicts their claim of discontinuous phase transition. On the other hand, Pouget and Launois [24] predicted the $M2$ to T transition as a continuous second-order transition from their calculation of negligible latent energy. To understand the nature of the structural phase transition, we plotted the normalized volume (based on the Z formula units per unit cell) as a function of pressure [Fig. 4(a)]. The normalized volume varies continuously with pressure, which resembles the previous reports [26,51]. The variation of lattice parameters also shows continuity as a function of pressure (Figs. Suppl-5(a)–5(c) [46]). Considering the thermodynamic parameter volume (V) as the order parameter of the structural transition, we calculated the first derivative of volume, bulk modulus $K = V(\mathrm{d}P/\mathrm{d}V)|_P$. The $K(P)$ vs P curve shows discontinuity

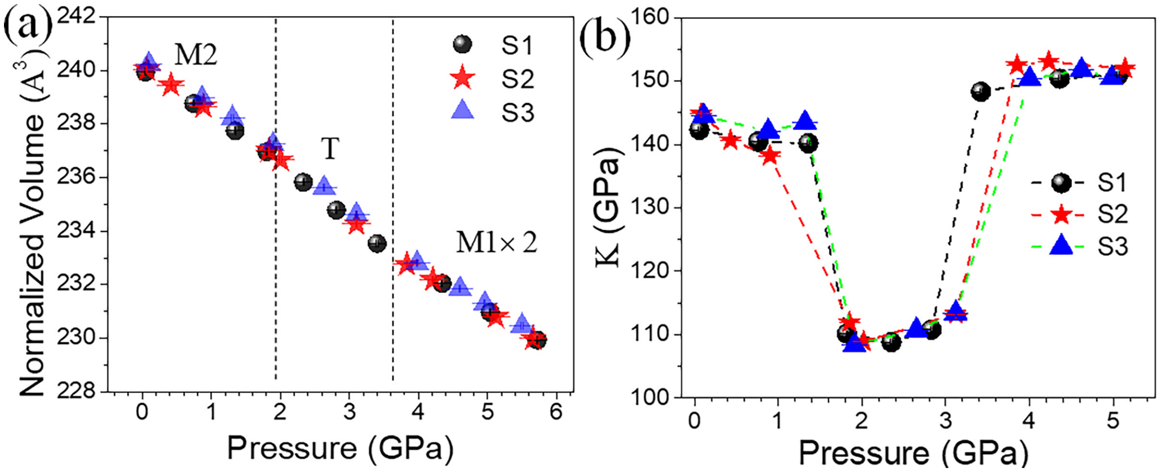

FIG. 4. Pressure dependence of the (a) unit-cell volume and (b) bulk modulus for all three samples.

around the phase transition [Fig. 4(b)]. The value of $K(P)$ for the $M2$ phase is ~140 GPa, which reduces to ~110 GPa for the T phase and again increases to ~150 GPa for the $M1$ phase of VO_2 [Fig. 4(b)]. We also found the values of bulk modulus K from the pressure vs volume plot in the individual phase fitted to a second-order Birch-Murnaghan equation (using EOSFIT7_GUI software) [52] (Figs. Suppl-6(a)–6(c) [46]). The bulk modulus values were obtained as 139.9 ± 2, 108.8 ± 2, and 148.3 ± 4 GPa for the $M2$, T, and $M1$ phases, respectively. The values of K match well with the reported values [38]. We have also calculated the bulk modulus using electronic density functional theory and the Voigt, Reuss, and Hill methods. The values for the bulk modulus were estimated as 257 ± 3 GPa for $M2$, 125 ± 4 GPa for T, and 254 ± 2 GPa for the $M1$ phase of VO_2. The deviation of the estimated values of the bulk modulus from the experimentally observed values may be because of the inherent nonstoichiometry in the oxide samples and the limitation of the methodology adopted in the present calculation. Moreover, in our study, three different phases appear with the short range of pressure variation. Thus we had no other choice except to fit the P-V data using a third-order polynomial with a 95% confidence interval (Fig. Suppl-7(a) [46]) for the calculation of the bulk modulus (Fig. Suppl-7(b) [46]), which is also used by others [38]. The calculated and experimentally observed values of the bulk modulus for the $M1$ and $M2$ phases are close to each other, whereas they decrease in the case of the T phase. The volume per formula unit is large in the case of the T phase and, thus, a lesser value of bulk modulus is expected than that for the $M1$ and $M2$ phases of VO_2. Given these results, the structural phase transitions from $M2$ to T and T to $M1$ are considered continuous second-order transitions. Our observation supports the negligible latent heat value for the $M2 \rightarrow T$ and $T \rightarrow M1$ transitions measured by Pouget *et al.* [5] using differential scanning calorimetry. The observed mixed-phase behavior in some reports may arise due to the coexistence of grains from both phases with a variation in strain [53,54].

To study the metal to insulator transition, we have carried out temperature-dependent Raman spectroscopic and XRD measurements of all the samples with different Mg concentrations. Figure 5(a) shows the Raman spectra for sample S1 with increasing and decreasing temperature. All the Raman modes disappeared at 358 K, confirming the transition to a metallic state [13]. With a decrease in temperature, the Raman modes reappear with a hysteresis of 15 K, confirming the reversibility of the phase transition.

Samples S2 and S3 also followed the same trend with a slight increase in transition temperature. The transition temperature for samples S2 and S3 are found to be 361 and 363 K, respectively. The variation of transition temperature with Mg concentration is shown in Fig. 5(b). The increase in transition temperature with Mg concentration can be explained by the finite-sized Heisenberg chains in the hole-doped systems, as explained in our previous reports [13,14]. We also carried out the temperature-dependent XRD measurements to examine the structural changes around MIT. Figure 6 shows the XRD patterns of sample S1 with increases and decreases in temperature. At room temperature (298 K), the samples maintain the M2 phase of VO_2 [23], whereas, with an increase (↑) in temperature to 343 K, the coexistence of both the $M2$ and R phases of VO_2 is observed [Fig. 6(a)]. With a further increase in temperature to 358 K, the XRD pattern resembles the pure R phase of VO_2, confirming the structural phase transition. With a decrease (↓) in temperature, the sample returns to its original $M2$ phase with a hysteresis of 25 K.

Samples S2 and S3 also followed the same trend with a slight increase in transition temperature (Figs. Suppl-8(a) and Suppl-8(b) [46]). We have plotted the diffraction pattern at lower 2θ values [Fig. 6(b)] with proper (hkl) notations to have a clear view of the coexistent phases. The coexistence of both the $M2$ and R phases for the narrow temperature range 343–348 K (with ↑ in temperature) and 322–328 K (with ↓ in temperature) confirms the $M2 \rightarrow R$ transition as a disorder-broadened first-order transition (Fig. 6).

In our earlier report [13], we showed that the electronic transition in VO_2 goes successively from three-band metallic to a single half-filled band, then to a 1D Heisenberg chain following Mott transition, and finally undergoes spin-Peierls dimerization. The first-order Mott-type MIT prompts SPT in VO_2. Figure Suppl-9 [46] shows the fitted third-order

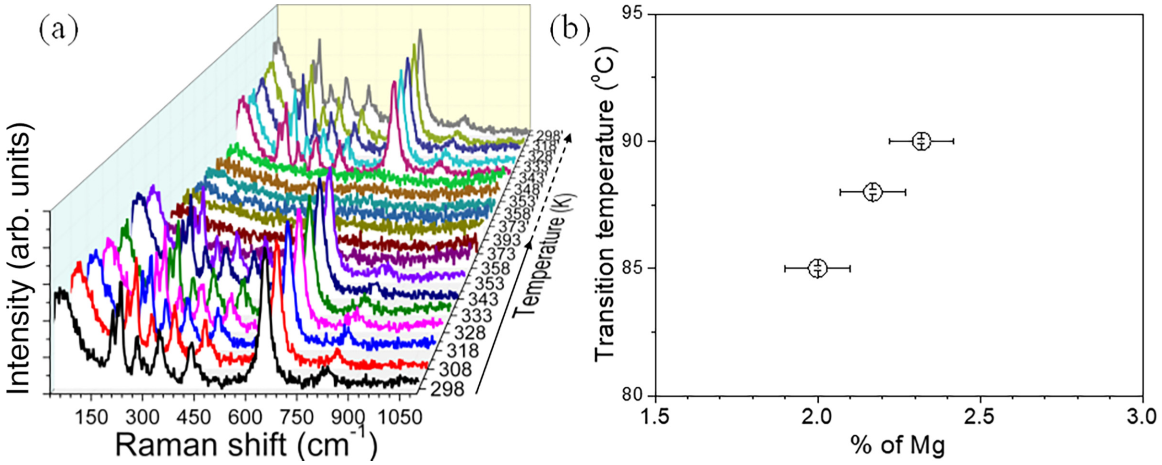

FIG. 5. (a) Raman spectra for sample S1 as a function of increasing and decreasing temperature. Solid and dashed arrows represent the increasing and decreasing temperature, respectively. Some of the data are reproduced from Basu *et al.* (Ref. [49]) with permission from AIP publishing. (b) Variation of transition temperature for the samples with Mg concentration.

Birch-Murnaghan equation of state curves for the R, $M1$, and $M2$ phases, where the minimum energy configurations are the ground states. We see that in the compressive strain or high-pressure regime, the $M2$ phase is stable as the volume decreases, while in the expansive strain or high-temperature regime, the $M1$ phase is stable as the volume increases. However, both the curves are quite close to each other with very small differences in the total energies, which implies that the transition between $M1$ and $M2$ can be continuous type (second order). The curve for the R phase is quite well separated and has a well-defined crossover point, which implies that the transition should occur in a sharp temperature range. However, for the T phase, we observed a curve similar to that of $M2$. The lower-symmetry $M1$ and T phases ($P21/c$ and $P\bar{1}$) are the maximal subgroups of the higher-symmetry $M2$ ($C2/m$) phase. Though the transition from R to $M2$ (MIT) is of first order (abrupt change between two space group symmetries), the strain-driven structural transitions between $M2$ and $M1/T$ are of second order (continuous symmetry breaking between the V-V dimers).

To understand the electronic and structural contribution to the phase transition, we have plotted the shift in Raman frequency with temperature for sample S1 (Fig. Suppl-10 [46]). All the Raman mode frequencies exhibit redshift with

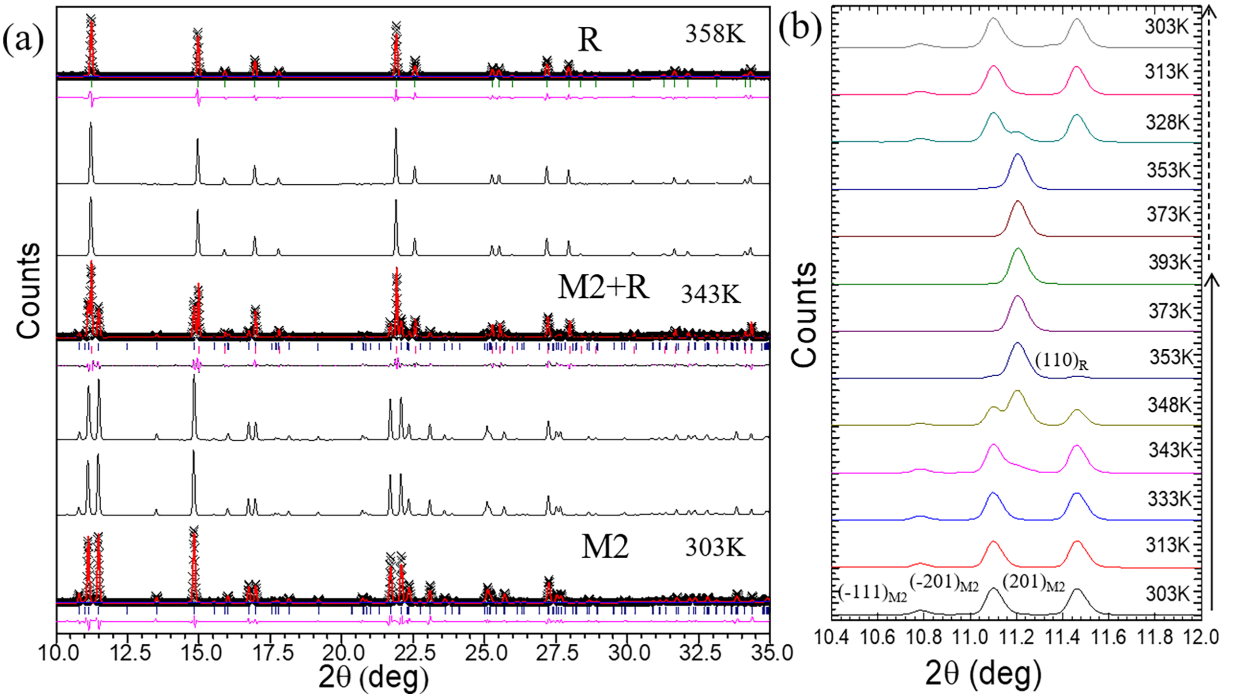

FIG. 6. (a) Refined XRD pattern for sample S1 as a function of temperature. The phases of VO_2 at the corresponding transition temperature are indicated. (b) Zoomed-in view of the XRD pattern at lower 2θ values with (hkl) indices showing the coexistence of the $M2$ and R phases of VO_2. Solid and dashed arrows represent the increasing and decreasing temperature, respectively.

increasing temperature. The maximum frequency shift is observed for the Raman band at 203 (V-V vibration) and 651 cm^{-1} (V-O vibration), indicating the reconstruction of V-V and V-O length along c_R [25,55]. We calculated the isobaric mode Grüneisen parameter $[\gamma_{iP} = (-1/\alpha\omega_i)(\mathrm{d}\omega_i/\mathrm{d}T)|_P]$, where α $(= 6 \times 10^{-6}\,\mathrm{K}^{-1})$ is the thermal expansion coefficient obtained from high-temperature XRD measurements, and it is close to the reported value of $5 \times 10^{-6}\,\mathrm{K}^{-1}$ [56]. We have observed that γ_{iP} values for the modes 203 and 217 cm^{-1} are higher compared to other mode frequencies (Table Suppl-III [46]). In our previous study, we showed that Raman modes at $\sim$200 cm^{-1} are due to V-V vibration as calculated from DFT phonon modeling [14]. The high value of γ_{iP} for these two modes compared to other frequencies confirms that the distortion along the c_R axis is responsible for the phase transition [26]. We performed the calculation to find out the contribution from explicit/true anharmonicity of the Raman modes for sample S1. We also measure the ratio (η) of γ_{iT} and γ_{iP} to find out the relative contribution of implicit (volume-dependent) and explicit (phonon-phonon interaction) anharmonicity. Table Suppl-III [46] lists the mode frequencies (ω_i) with the corresponding γ_{iT} and γ_{iP} along with η $(= \gamma_{iT}/\gamma_{iP})$ [57]. For all the Raman modes, the value of $\eta \ll 1$, which implies most of the contribution is due to explicit anharmonicity. A similar trend is also observed for samples S2 and S3. From the above observations, it is clear that the frequency shift is dominated by phonon-phonon interaction, and the coexistence of both phases confirms the $M2 \rightarrow R$ transition as the first order. Our observation supports the high latent heat value (770 cal/mole) for the $M2 \rightarrow R$ transition measured by Pouget and Launois [24] using differential scanning calorimetry. We have also plotted the mode Grüneisen parameters as a function of doping. The maximum change in the anharmonic parameters is observed for the mode frequency 203 cm^{-1} (V-V vibration along the c_R direction). Doping Mg in VO_2 stabilizes the $M2$ phase by introducing tensile strain along the c_R direction. The more doping there is, the higher is the magnitude of strain. The contribution of doping on isobaric (γ_{iP}, phonon-phonon interaction) anharmonicity compared to isothermal (γ_{iT}, volume contribution) anharmonicity is thus expected.

IV. CONCLUSIONS

$\mathrm{V}_{1-x}\mathrm{Mg}_x\mathrm{O}_2$ samples were grown in stable $M2$ phases of VO_2 by controlled doping of Mg. Pressure-induced structural phase transitions from the $M2 \rightarrow T \rightarrow M1$ phases of VO_2 are observed in both XRD and Raman spectroscopic studies. The transition pressure for $M2 \rightarrow T$ and $T \rightarrow M1$ are observed to increase with the increase in doping concentration following the phase diagram of VO_2. The structural transitions $M2 \rightarrow T$ and $T \rightarrow M1$ are found to be a second-order continuous phase transition from the continuous change in the volume and a discontinuity in the bulk modulus with quasihydrostatic pressure. However, the temperature-driven $M2 \rightarrow R$ phase transition is found as a disorder-broadened first-order type from the coexistence of both phases for a narrow span of temperature along with a hysteresis of 25 K. We argue that Mott-type first-order metal to insulator transition prompts the MIT from R to $M2$, whereas a second-order structural relaxation leads to the transition from $M2$ to $M1$ via the T phase. Further, the pressure- and temperature-dependent Raman spectroscopic studies help in finding the isothermal and isobaric Grüneisen parameters for the phonon modes and their relative contribution towards thermal expansion. Phonon-phonon interaction is found to be dominant over the implicit (volume-dependent) anharmonicity for the structural transitions.

ACKNOWLEDGMENTS

We thank Shradhanjali Sahoo of the Condensed Matter Physics Division, Indira Gandhi Centre for Atomic Research, for her help in pressure-dependent Raman studies. We acknowledge the Director, Indira Gandhi Centre for Atomic Research for his encouragement.

---

[1] F. J. Morin, Oxides which show a metal-to-insulator transition at the Néel temperature, Phys. Rev. Lett. **3**, 34 (1959).

[2] M. W. Haverkort, Z. Hu, A. Tanaka, W. Reichelt, S. V. Streltsov, M. A. Korotin, V. I. Anisimov, H. H. Hsieh, H. -J. Lin, C. T. Chen, D. I. Khomskii, and L. H. Tjeng, Orbital-assisted metal-insulator transition in VO_2, Phys. Rev. Lett. **95**, 196404 (2005).

[3] H.-T. Kim, Y. W. Lee, B.-J. Kim, B.-G. Chae, S. J. Yun, K.-Y. Kang, K.-J. Han, K.-J. Yee, and Y.-S. Lim, Monoclinic and correlated metal phase in VO_2 as evidence of the Mott transition: Coherent phonon analysis, Phys. Rev. Lett. **97**, 266401 (2006).

[4] E. Strelcov, A. Tselev, I. Ivanov, J. D. Budai, J. Zhang, J. Z. Tischler, I. Kravchenko, S. V. Kalinin, and A. Kolmakov, Doping-based stabilization of the $M2$ phase in free-standing VO_2 nanostructures at room temperature, Nano Lett. **12**, 6198 (2012).

[5] J. P. Pouget, H. Launois, J. P. D'Haenens, P. Merenda, and T. M. Rice, Electron localization induced by uniaxial stress in pure VO_2, Phys. Rev. Lett. **35**, 873 (1975).

[6] J. H. Park, J. M. Coy, T. S. Kasirga, C. Huang, Z. Fei, S. Hunter, and D. H. Cobden, Measurement of a solid-state triple point at the metal-insulator transition in VO_2, Nature (London) **500**, 431 (2013).

[7] M. Marezio, P. D. Dernier, and A. Santoro, Twinning in Cr-doped VO_2, Acta Crystallogr. **A29**, 618 (1973).

[8] G. Villeneuve, M. Drillon, P. Hagenmuller, M. Nygren, J. P. Pouget, F. Carmona, and P. Delhaes, Magnetic and structural properties of stoichiometric and non-stoichiometric (V, Al) O_2 alloys, J. Phys. C: Solid State Phys. **10**, 3621 (1977).

[9] W. Brückner, U. Gerlach, W. Moldenhauer, H. P. Brückner, N. Mattern, H. Oppermann, and E. Wolf, Phase transitions and semiconductor-metal transition in $\mathrm{V}_{1-x}\mathrm{Ga}_x\mathrm{O}_2$ single crystals, Phys. Status Solidi A **38**, 93 (1976).

[10] A. Zylbersztejn and N. F. Mott, Metal-insulator transition in vanadium dioxide, Phys. Rev. B **11**, 4383 (1975).

[11] J. B. Goodenough, The two components of the crystallographic transition in VO_2, J. Solid State Chem. **3**, 490 (1971).

[12] V. Eyert, The metal-insulator transitions of VO_2: A band theoretical approach, Ann. Phys. (Leipzig) **514**, 650 (2002).

[13] R. Basu, M. Sardar, S. Bera, P. Magudapathy, and S. Dhara, The role of 1-D finite size Heisenberg chains in increasing the metal

to insulator transition temperature in hole rich VO_2, Nanoscale **9**, 6537 (2017).

[14] R. Basu, V. Srihari, M. Sardar, S. K. Srivastava, S. Bera, and S. Dhara, Probing phase transition in VO_2 with the novel observation of low-frequency collective spin excitation, Sci. Rep. **10**, 1977 (2020).

[15] D. H. Kim and H. S. Kwok, Pulsed laser deposition of VO_2 thin films, Appl. Phys. Lett. **65**, 3188 (1994).

[16] N. Mlyuka, G. Niklasson, and C.-G. Granqvist, Mg doping of thermochromic VO_2 films enhances the optical transmittance and decreases the metal-insulator transition temperature, Appl. Phys. Lett. **95**, 171909 (2009).

[17] W. R. Roach, Holographic storage in VO_2, holographic storage in VO_2, Appl. Phys. Lett. **19**, 453 (1971).

[18] S. Lu, L. Hou, and F. Gan, Preparation and optical properties of phase-change VO_2 thin films, J. Mater. Sci. **28**, 2169 (1993).

[19] T. M. Rice, H. Launois, and J. P. Pouget, Comment on "VO_2: Peierls or Mott-Hubbard? A view from band theory, Phys. Rev. Lett. **73**, 3042 (1994).

[20] S. Zhang, J. Y. Chou, and L. J. Lauhon, Direct correlation of structural domain formation with the metal insulator transition in a VO_2 nanobeam, Nano Lett. **9**, 4527 (2009).

[21] R. M. Wentzcovitch, VO_2: Peierls or Mott-Hubbard? A view from band theory, Phys. Rev. Lett. **72**, 3389 (1994).

[22] J. Goodenough and H. Y. Hong, Structures and a two-band model for the system $V_{1-x}Cr_xO_2$, Phys. Rev. B **8**, 1323 (1973).

[23] C. Sommers and S. Doniach, First principles calculation of the intra-atomic correlation energy in VO_2, Solid State Commun. **28**, 133 (1978).

[24] J. P. Pouget and H. Launois, Dimerization of a linear Heisenberg chain in the insulating phases of $V_{1-x}Cr_xO_2$, Phys. Rev. B **10**, 1801 (1974).

[25] J. P. D'Haenens, D. Kaplan, and P. Merenda, Electron spin resonance in $V_{1-x}Cr_xO_2$, J. Phys. C **8**, 2267 (1975).

[26] R. Basu, A. Patsha, S. Chandra, S. Amirthapandian, K. G. Raghavendra, A. Dasgupta, and S. Dhara, Polarized tip-enhanced Raman spectroscopy in understanding metal to insulator and structural phase transition in VO_2, J. Phys. Chem. C **123**, 11189 (2019).

[27] J. M. Atkin, S. Berweger, E. K. Chavez, M. B. Raschke, J. Cao, W. Fan, and J. Wu, Strain and temperature dependence of the insulating phases of VO_2 near the metal-insulator transition, Phys. Rev. B **85**, 020101(R) (2012).

[28] C. Chen, Y. Zhao, X. Pan, V. Kuryatkov, A. Bernussi, M. Holtz, and Z. Fan, Influence of defects on structural and electrical properties of VO_2 thin films, J. Appl. Phys. **110**, 023707 (2011).

[29] S. Lee, C. Cheng, H. Guo, K. Hippalgaonkar, K. Wang, J. Suh, K. Liu, and J. Wu, Axially engineered metal-insulator phase transition by graded doping VO_2 nanowires, J. Am. Chem. Soc. **135**, 4850 (2013).

[30] W. Brückner, U. Gerlach, and B. Thuss, Phase diagram of $V_{1-x}Al_xO_2$, Phys. Status Solidi A **40**, K131 (1977).

[31] B. Fisher, Electrical and seebeck effect measurements in Nb doped VO_2, J. Phys. Chem. Solids **43**, 205 (1982).

[32] B. Rajeswaran and A. M. Umarji, Effect of W addition on the electrical switching of VO_2 thin films, AIP Adv. **6**, 035215 (2016).

[33] E. K. Barimah, A. Boontan, D. P. Steenson, and G. Jose, Infrared optical properties modulation of VO_2 thin film fabricated by ultrafast pulsed laser deposition for thermochromic smart window applications, Sci. Rep. **12**, 11421 (2022).

[34] A. K. Prasad, S. Amirthapandian, S. Dhara, S. Dash, N. Murali, and A. K. Tyagi, Novel single phase vanadium dioxide nanostructured films for methane sensing near room temperature, Sens. Actuators B **191**, 252 (2014).

[35] C. Nethravathi, C. R. Rajamathi, M. Rajamathi, U. K. Gautam, X. Wang, D. Golberg, and Y. Bando, N-doped graphene $-VO_2$ (B) nanosheet-built 3D flower hybrid for lithium ion battery, ACS Appl. Mater. Interfaces **5**, 2708 (2013).

[36] H.-T. Kim, B.-G. Chae, D.-H. Youn, G. Kim, and K.-Y. Kang, Raman study of electric-field-induced first-order metal-insulator transition in VO_2-based devices, Appl. Phys. Lett. **86**, 242101 (2005).

[37] M. Mitrano, B. Maroni, C. Marini, M. Hanfland, B. Joseph, P. Postorino, and L. Malavasi, Anisotropic compression in the high-pressure regime of pure and chromium-doped vanadium dioxide, Phys. Rev. B **85**, 184108 (2012).

[38] C. Marini, E. Arcangeletti, D. D. Castro, L. Baldassare, A. Perucchi, S. Lupi, L. Malavasi, L. Boeri, E. Pomjakushina, K. Conder, and P. Postorino, Optical properties of $V_{1-x}Cr_xO$ compounds under high pressure, Phys. Rev. B **77**, 235111 (2008).

[39] A. P. Hammersley, S. O. Svensson, M. Hanfland, A. N. Fitch, and D. Häusermann, Two-dimensional detector software: from real detector to idealised image or two-theta scan, High Press. Res. **14**, 235 (1996).

[40] G. J. Piermarini, S. Block, J. D. Barnett, and R. A. Forman, Calibration of the pressure dependence of the $R1$ ruby fluorescence line to 195 kbar, J. Appl. Phys. **46**, 2774 (1975).

[41] S. Klotz, Hydrostatic limits of 11 pressure transmitting media, J. Phys. D: Appl. Phys. **42**, 075413 (2009).

[42] G. Kresse and J. Hafner, *Ab initio* molecular dynamics for liquid metals, Phys. Rev. B **47**, 558 (1993).

[43] G. Kresse and J. Furthmüller, Efficient iterative schemes for *ab initio* total-energy calculations using a plane-wave basis set, Phys. Rev. B **54**, 11169 (1996).

[44] M. Marezio, D. B. McWhan, J. P. Remeika, and P. D. Dernier, Structural aspects of the metal-insulator transitions in Cr-doped VO_2, Phys. Rev. B **5**, 2541 (1972).

[45] R. Srivastava and L. Chase, Raman spectrum of semiconducting and metallic VO_2, Phys. Rev. Lett. **27**, 727 (1971).

[46] See Supplemental Material at http://link.aps.org/supplemental/10.1103/PhysRevB.109.184107 for XPS analysis, and temerature and pressure dependent Raman and XRD data for all the samples. Detailed structural analysis and calculated mode Gruneisen parameters are also provided here.

[47] P. Schilbe, Raman scattering in VO_2, Phys. B: Condens. Matter **316**, 600 (2002).

[48] K. Kamali, T. R. Ravindran, C. Ravi, Y. Sorb, N. Subramanian, and A. K. Arora, Anharmonic phonons of $NaZr_2(PO_4)_3$ studied by Raman spectroscopy, first-principles calculations, and x-ray diffractions, Phys. Rev. B **86**, 144301 (2012).

[49] R. Basu, K. K. Mishra, T. R. Ravindran, and S. Dhara, High pressure spectroscopic studies of phase transition in VO_2, AIP Conf. Proc. **1951**, 030012 (2018).

[50] H. Zhang, Q. Li, B. Cheng, Z. Guan, R. Liu, B. Liu, Z. Liu, X. Li, T. Cui, and B. Liu, The pressure-induced metallization of monoclinic vanadium dioxide, RSC Adv. **6**, 104949 (2016).

[51] F. Birch, Finite strain isotherm and velocities for single-crystal and polycrystalline NaCl at high pressures and 300 °K, J. Geophys. Res. **83**, 1257 (1978).

[52] A. C. Jones, S. Berweger, J. Wei, D. Cobden, and M. B. Raschke, Nano-optical investigations of the metal−insulator phase behavior of individual VO_2 microcrystals, Nano Lett. **10**, 1574 (2010).

[53] J. I. Sohn, H. J. Joo, D. Ahn, H. H. Lee, A. E. Porter, K. Kim, D. J. Kang, and M. E. Welland, Surface-stress-induced Mott transition and nature of associated spatial phase transition in single crystalline VO_2, Nano Lett. **9**, 3392 (2009).

[54] K. Okimura, T. Watanabe, and J. Sakai, Stress-induced VO_2 films with $M2$ monoclinic phase stable at room temperature grown by inductively coupled plasma-assisted reactive sputtering, J. Appl. Phys. **111**, 073514 (2012).

[55] A. Rúa, R. Cabrera, H. Coy, E. Merced, N. Sepúlveda, and F. E. Fernández, Phase transition behavior in microcantilevers coated with $M1$-phase VO_2 and $M2$-phase VO_2:Cr thin films, J. Appl. Phys. **111**, 104502 (2012).

[56] G. V. Chandrashekhar, H. L. C. Barros, and J. M. Honig, Heat capacity of VO_2 single crystals, Mater. Res. Bull. **8**, 369 (1973).

[57] S. Samanta, Q. Li, B. Cheng, Y. Huang, C. Pei, Q. Wang, Y. Ma, and L. Wang, Phase coexistence and pressure-temperature phase evolution of VO_2 nanorods near the semiconductor-semiconductor transition, Phys. Rev. B **95**, 045135 (2017).